Precision Measurement of the Excited State Landé g-factor and Diamagnetic Shift of the Cesium D₂ Line

Hans Stærkind[1,2,*] Kasper Jensen[1,3] Jörg H. Müller[1] Vincent O. Boer[2]
Esben T. Petersen[2,4] and Eugene S. Polzik[1]

[1]*Niels Bohr Institute, University of Copenhagen, Blegdamsvej 17, 2100 Copenhagen, Denmark*
[2]*Danish Research Centre for Magnetic Resonance, Centre for Functional and Diagnostic Imaging and Research, Copenhagen University Hospital—Amager and Hvidovre, Kettegård Allé 30, 2650 Hvidovre, Denmark*
[3]*School of Physics and Astronomy, University of Nottingham, University Park, Nottingham NG7 2RD, United Kingdom*
[4]*Section for Magnetic Resonance, DTU-Health Tech, Technical University of Denmark, Oersteds Plads, Building 349, 1st floor, 2800 Kgs Lyngby, Denmark*

Transitions between the extreme angular-momentum states of alkali D lines hold the potential for enabling accurate high-field optical magnetometry because of their very simple magnetic field dependence described only by a linear and a quadratic term, characterized by the two coefficients γ_1 and γ_2. Here, we present very accurate measurements of these coefficients, for the cesium D₂ line, thereby overcoming a major obstacle for the realization of this future technology. By means of saturated absorption spectroscopy on a cesium gas, in 3 T and 7 T magnetic fields, we measure the linear magnetic frequency shift of the transition to be $\gamma_1 = 13.994\,301(11)$ GHz/T. This measurement corresponds to an optical magnetic field determination of better than 1 ppm accuracy. From this value, we can calculate the fine-structure Landé g-factor $g_J(6^2P_{3/2}) = 1.334\,087\,49(52)$. This result is consistent with the previous best measurement, and it improves the accuracy by more than 2 orders of magnitude. We also measure, for the first time, the quadratic diamagnetic shift as $\gamma_2 = 0.4644(35)$ MHz/T². Our work opens up the field of accurate high-field optical magnetometry using atomic cesium, with possible applications in, e.g., medical MRI, fusion reactors, and particle accelerators. These high-accuracy measurements also allow for testing of advanced atomic structure models, as our results are incompatible with the Russel-Saunders coupling value and the hydrogen-constant-core-model value by 31 and 7 standard deviations, respectively.

Subject Areas: Atomic and Molecular Physics, Optics

I. INTRODUCTION

The field of optical magnetometry has undergone rapid development during the last couple of decades [1]. While devices for measuring tiny magnetic fields have matured to the point of emerging practical applications, e.g., magneto-cardiography and magnetoencephalography [2–5], optical magnetometers for high magnetic fields are still at a less advanced level.

Low-field optical magnetometry typically works by optical detection of the Larmor precession of optically pumped atomic spins [1]. High-field optical magnetometers,

on the other hand, usually rely on measuring the Zeeman shift of the optical absorption lines. Much of the work is focused on the D lines of alkali vapors [6–9]. In other work, not directly aimed at magnetometry applications, (non-linear) spectroscopy and optical pumping of alkali atoms in high magnetic fields have been studied [10–15].

Currently, accurate measurements of magnetic fields in the tesla range are typically performed using nuclear magnetic resonance (NMR) spectroscopy on protons in water [16]. NMR measurements are highly sensitive but require the application and detection of radio frequency (rf) magnetic pulses. Optical magnetometry provides a completely different way of measuring high magnetic fields, with advantages such as continuous and fast readout without rf, electronic, or metallic components in the field probe. Optical magnetometry also allows for remote detection, e.g., measurements on exploding wires [17–20] and sunspots [21]. Indeed, the observation of sodium line splitting in sunspots dates all the way back to 1870 [22].

*hans.staerkind@nbi.ku.dk

On Earth, high magnetic fields are found in magnetic resonance imaging (MRI) scanners, NMR spectrometers, particle accelerators, fusion reactors, and a range of advanced physics experiments [23].

A major roadblock for the practical use of optical magnetometry for high fields is currently the accuracy with which the excited state g-factors of the alkali D lines are known [7,23]. In order to enable accurate high-field optical magnetometry, we here present an improved measurement of the excited state Landé g-factor for the cesium D_2 line, along with the first-ever measurement of the diamagnetic shift of this line. By using a 3 T and a 7 T MRI scanner, we have very stable and homogeneous high magnetic fields and, at the same time, all the hardware needed to accurately determine these fields using NMR spectroscopy. To determine optical frequency shifts in these fields, we realize saturated absorption spectroscopy inside the MRI scanners. By combining NMR and optical measurements, more than 2 orders-of-magnitude improvement in accuracy is achieved for the excited state g-factor, compared to previous work.

The data presented here also surpass the accuracy of published theoretical values from atomic structure calculations. Hence, as a spin-off, our data can be used to test advanced atomic structure models.

II. SPLITTING OF THE D_2 LINE

We consider the transition from the cesium-133 ground state $6^2S_{1/2}$ to the excited state $6^2P_{3/2}$, known as the D_2 line. With saturated absorption spectroscopy, the limitation of Doppler broadening is surpassed, and the hyperfine splitting of this line can readily be resolved [24]. In the following, we review how the line splitting depends on an applied magnetic field in the tesla range. We consider the Zeeman interaction in detail and simply take the hyperfine shift to be

$$\Delta E_{\text{HFS}} = \frac{1}{2}A\big(F(F+1) - I(I+1) - J(J+1)\big). \quad (1)$$

Here, F, I, and J are the atomic, nuclear, and electronic total angular-momentum quantum numbers, respectively. The magnetic dipole hyperfine coupling constant A is $h \times 2.298\,1579\,425\,\text{GHz}$ for the ground state [25,26], and $h \times 50.288\,27(23)\,\text{MHz}$ for the excited state [26,27], where h is the Planck constant [28]. For a more detailed treatment of the hyperfine structure including electric quadrupole and magnetic octupole interactions, which are not relevant to the results in this work, see Refs. [25–27,29].

A. Zeeman shift

As described in Refs. [25,26,29], the Zeeman shift of a state can be written as

$$\Delta E_{\text{Z}} = (g_S m_S + g_L m_L + g_I m_I)\mu_{\text{B}}B. \quad (2)$$

Here, g_S and g_L are the electron spin and orbital g-factors, respectively, and g_I is the nuclear g-factor. Additionally, m_S, m_L, and m_I are the electron spin, electron orbital, and nuclear projected angular-momentum quantum numbers, respectively; μ_{B} is the Bohr magneton [28]; and B is the magnitude of the magnetic field whose direction defines the quantization axis. In the following, B is referred to simply as the magnetic field. We include a finite nuclear mass correction for the orbital g-factor, $g_L = m_{\text{N}}/(m_{\text{N}} + m_{\text{e}}) \approx 1 - m_{\text{e}}/m_{\text{N}}$ [26,29,30]. Here, m_{e} is the electron mass, and m_{N} is the nuclear mass. Equation (2) is the appropriate equation to use in the case of kilotesla fields, i.e., in the fine Paschen-Back regime, where the Zeeman shift is large compared to the fine structure. For a Zeeman shift that is small compared to the fine structure but large compared to the hyperfine structure, i.e., in the hyperfine Paschen-Back regime, where our two MRI scanners operate, we can write the shift as

$$\Delta E_{\text{Z}} = (g_J m_J + g_I m_I)\mu_{\text{B}}B, \quad (3)$$

with the Landé g-factor g_J approximately given by the Russell-Saunders (RS) coupling value [26,29,30]

$$g_J = g_L \frac{J(J+1) - S(S+1) + L(L+1)}{2J(J+1)}$$
$$+ g_S \frac{J(J+1) + S(S+1) - L(L+1)}{2J(J+1)}. \quad (4)$$

Here, S and L are the total electronic spin and orbital angular-momentum quantum numbers, respectively. When the Zeeman shift is small compared to the hyperfine structure, i.e., in the Zeeman regime, we can write the shift as

$$\Delta E_{\text{Z}} = g_F m_F \mu_{\text{B}}B, \quad (5)$$

with the Landé g-factor g_F as given in Ref. [26] and m_F being the atomic projected angular-momentum quantum number.

Numerically diagonalizing the total Hamiltonian composed of the hyperfine Hamiltonian, equivalent to Eq. (1), and the Zeeman Hamiltonian, equivalent to Eq. (3), and ignoring the small nuclear Zeeman interaction $g_I m_I \mu_{\text{B}}B$, we can visually inspect the magnetic field dependence of the states as we transition from the Zeeman regime into the hyperfine Paschen-Back regime. This magnetic field dependence is shown for the ground and excited states in Figs. 1(a) and 1(b), respectively. Groups of states are labeled with quantum numbers; primes are used for excited state quantum numbers. Notice how the Zeeman interaction acts as a perturbation to the hyperfine splitting at low fields, breaking the degeneracy of the different m_F states. At high
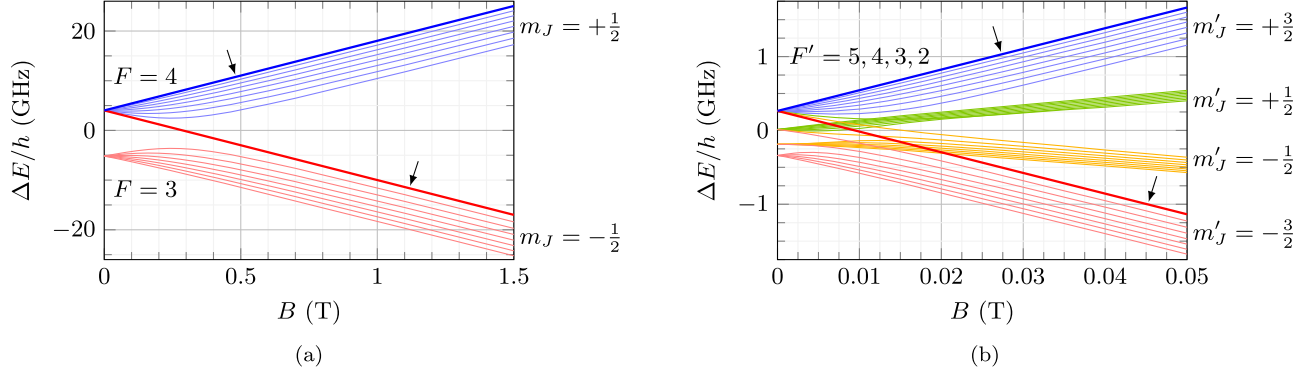
FIG. 1. Energy splitting for the ground and excited states, as a function of applied magnetic field. The two different magnetic field axes are chosen to highlight the evolution from the Zeeman regime to the hyperfine Paschen-Back regime for the two states. (a) Ground state, $6^2S_{1/2}$, energy splitting. The bold blue line is the $|F, m_F\rangle = |4, 4\rangle$ state, and the bold red line is the $|4, -4\rangle$ state. Both are marked with arrows. (b) Excited state, $6^2P_{3/2}$, energy splitting. The bold blue line is the $|F', m'_F\rangle = |5, 5\rangle$ state, and the bold red line is the $|5, -5\rangle$ state. Both are marked with arrows.

fields, the hyperfine interaction acts as a perturbation to the Zeeman splitting breaking the degeneracy of the eight m_I states, $-\frac{7}{2}$ to $+\frac{7}{2}$. The hyperfine Paschen-Back regime occurs at different magnetic fields due to the different hyperfine coupling constants of the ground and excited states, and it continues well beyond the 7 T relevant for this study.

B. Extreme angular-momentum states

Now, we turn our attention to the σ_+ transition between the extreme angular-momentum states, i.e., the transition between the ground state with maximum total and projected angular momenta, $|F, m_F\rangle = |4, 4\rangle$, and the excited state with maximum total and projected angular momenta, $|F', m'_F\rangle = |5, 5\rangle$. We call this the extreme σ_+ transition. The two states of this transition do not mix with any of the other angular-momentum states when we transition from the Zeeman regime to the hyperfine Paschen-Back regime and ultimately into the fine Paschen-Back regime. The labeling of the two states in the different regimes is summarized in Table I. Notice that, for both states, the projected angular-momentum quantum numbers are equal to the corresponding total angular-momentum quantum numbers, and the sums of all the projected angular-momentum quantum numbers are the same in all regimes. The frequency shifts of these states are linearly dependent

on the magnetic field in all regimes and also in the intermediate regimes. Hence, the extreme σ_+ transition is also linearly dependent on the magnetic field.

In Fig. 2, $\sigma_\pm$ transitions in the hyperfine Paschen-Back regime are shown, along with their extensions into the Zeeman regime. The electric-dipole-allowed strong $\sigma_\pm$ transitions are those obeying the selection rules $\Delta m_J = \pm 1$ [31] and, by conservation of angular momentum, $\Delta m_I = 0$. The extreme σ_+ transition is highlighted in bold blue. The weaker transitions with $\Delta m_I = \pm 1$, forbidden in the high-field limit, are also shown.

Highlighted in bold red in Fig. 2 is the extreme σ_- transition $|4, -4\rangle \leftrightarrow |5, -5\rangle$, i.e., the transition between the
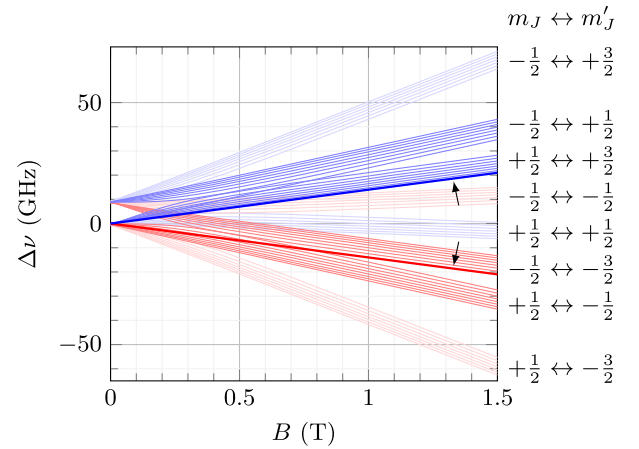

FIG. 2. Splitting of the D_2 line in a magnetic field. The blue lines correspond to σ_+ transitions; the red lines correspond to σ_- transitions. The bold blue line is the extreme σ_+ transition. The bold red line is the extreme σ_- transition. Both lines are marked with arrows. Light-colored lines correspond to the weak transitions with $\Delta m_I = \pm 1$. The shifts $\Delta \nu$ are relative to the extreme $\sigma_\pm$ transitions at 0 T. To the right of the figure, we give the ground state m_J and excited state m'_J for the transitions.

TABLE I. Labeling of the extreme angular-momentum states in the three regimes.

	Zeeman	Hyperfine Paschen-Back	Fine Paschen-Back
	$|F, m_F\rangle$	$|J, m_J, I, m_I\rangle$	$|L, m_L, S, m_S, I, m_I\rangle$
Ground state	$|4, 4\rangle$	$\left|\frac{1}{2}, \frac{1}{2}, \frac{7}{2}, \frac{7}{2}\right\rangle$	$\left|0, 0, \frac{1}{2}, \frac{1}{2}, \frac{7}{2}, \frac{7}{2}\right\rangle$
Excited state	$|5, 5\rangle$	$\left|\frac{3}{2}, \frac{3}{2}, \frac{7}{2}, \frac{7}{2}\right\rangle$	$\left|1, 1, \frac{1}{2}, \frac{1}{2}, \frac{7}{2}, \frac{7}{2}\right\rangle$

negative extreme angular-momentum states, which is similarly linearly dependent on the magnetic field (but with the opposite sign) and has the same transition frequency at 0 T.

An experimental overview confirming the splitting pattern in Fig. 2, from 0 T to 1.5 T, is presented in Appendix H. This range of magnetic fields highlights the evolution from the Zeeman regime to the hyperfine Paschen-Back regime.

By expanding the atomic Hamiltonian accounting for the momentum of the magnetic field, a term quadratic in the magnetic field appears [7,32–35]. This is the diamagnetism of the atom, and for non-Rydberg states, it is typically neglected since it is much smaller than the linear term. For our purpose, however, we cannot neglect it, and thus, the linear shift of the two extreme transitions is supplemented by a quadratic one [not shown in Figs. 1(a), 1(b), and 2]. The expected coefficient ξ^{dia} to the quadratic term, within the hydrogen-constant-core-model (HCCM), is given by

$$\xi^{\mathrm{dia}} = \frac{5e^2 a_0^2}{8m_\mathrm{e}} \left(1 + \frac{1 - 3L(L+1)}{5(n^*)^2}\right)$$
$$\times \frac{L(L+1) + m_L^2 - 1}{(2L-1)(2L+3)} (n^*)^4, \tag{6}$$

following the conventions of Ref. [7]. Here, n^* is the effective principal quantum number [7,36], e is the electron charge, a_0 is the Bohr radius, and m_e is the electron mass [28]. Using the reduced electron mass, due to the finite nuclear mass, is not relevant for the first five digits. The quadratic dependence on m_L implies that this shift, including the sign, is the same for the two extreme transitions.

The resulting model constitutes a good operational description of the magnetic field dependence of the extreme transitions, making them highly useful for accurate magnetometry as described in the next section.

III. HIGH-FIELD MAGNETOMETRY WITH CESIUM

Using Eq. (3) and (6), the magnetic-field-dependent frequency shifts are, for the positive and negative extreme angular-momentum ground states,

$$\Delta \nu_{\mathrm{g}\pm} = \pm (g_J(6^2 S_{1/2}) \cdot 1/2 + g_I \cdot 7/2) \frac{\mu_\mathrm{B}}{h} B + \frac{\xi_\mathrm{g}^{\mathrm{dia}}}{h} B^2, \tag{7}$$

and for the positive and negative extreme angular-momentum excited states,

$$\Delta \nu_{\mathrm{e}\pm} = \pm (g_J(6^2 P_{3/2}) \cdot 3/2 + g_I \cdot 7/2) \frac{\mu_\mathrm{B}}{h} B + \frac{\xi_\mathrm{e}^{\mathrm{dia}}}{h} B^2. \tag{8}$$

Notice how the nuclear Zeeman shifts of the two states involved in each of the two extreme transitions are the same, so they do not contribute to the magnetic field dependence of the transitions,

$$\Delta \nu_\pm = \Delta \nu_{\mathrm{e}\pm} - \Delta \nu_{\mathrm{g}\pm}$$
$$= \pm (g_J(6^2 P_{3/2}) \cdot 3/2 - g_J(6^2 S_{1/2}) \cdot 1/2) \frac{\mu_\mathrm{B}}{h} B$$
$$+ \frac{1}{h} (\xi_\mathrm{e}^{\mathrm{dia}} - \xi_\mathrm{g}^{\mathrm{dia}}) B^2. \tag{9}$$

Defining, for simplicity,

$$\gamma_1 \equiv \frac{\mu_\mathrm{B}}{h} (g_J(6^2 P_{3/2}) \cdot 3/2 - g_J(6^2 S_{1/2}) \cdot 1/2), \tag{10}$$

$$\gamma_2 \equiv \frac{1}{h} (\xi_\mathrm{e}^{\mathrm{dia}} - \xi_\mathrm{g}^{\mathrm{dia}}), \tag{11}$$

we find

$$\Delta \nu_\pm = \pm \gamma_1 B + \gamma_2 B^2. \tag{12}$$

In practice, for fields in the tesla range, it is useful to modify this expression to

$$\Delta \nu_\pm = \gamma_0 \pm \gamma_1 \zeta B + \gamma_2 \zeta^2 B^2, \tag{13}$$

where γ_0 is an experimental offset in the frequency shift measurement, and ζ is a factor describing the magnetic field shift introduced by the magnetic susceptibility of the probe—that is, the structure containing the cesium vapor—such that B is defined as the magnetic field in the absence of the probe. Ideally, the offset γ_0 should be small compared to the linewidth of the transition, and the probe field shift ζ should deviate from 1 only by a few ppm.

Using this relation, accurate high-field magnetometry can be performed by measuring the optical frequency shifts $\Delta \nu_\pm$. However, knowledge of γ_1 is limited by the large uncertainty on the excited state Landé g-factor $g_J(6^2 P_{3/2})$, and neither γ_2 nor its constituents have ever been measured before.

In order to enable accurate high-field magnetometry with cesium, we here present a highly improved measurement of γ_1, and therefore also of $g_J(6^2 P_{3/2})$. We also present a first-ever measurement of γ_2.

IV. CURRENT BEST NUMBERS

The value for the cesium ground state Landé g-factor is, according to Ref. [25], determined from experimental data as 2.002 540 32(20). This calculation is based on accurate measurements of the free electron g-factor $g(e)$; the ratio

between the rubidium ground state and the free electron g-factors, $g_J(\text{Rb})/g(e)$; and the ratio between the cesium and the rubidium ground state g-factors, $g_J(\text{Cs})/g_J(\text{Rb})$. As shown in Refs. [6,7] for rubidium, we recalculate with updated values for $g(e)$ [28] and $g_J(\text{Rb})/g(e)$ [37] to arrive at

$$g_J(6^2S_{1/2}) = 2.002\,540\,261(27). \qquad (14)$$

This result is an order-of-magnitude improvement in accuracy compared to the value in Ref. [25]. This value is the current best estimate of the ground state g-factor.

From Refs. [25,26], the best measurement of the excited state Landé g-factor is

$$g_J(6^2P_{3/2}) = 1.334\,00(30), \qquad (15)$$

as measured by Abele *et al.* in 1975 [38].

A theoretical value for the Landé g-factor, $g_J(6^2P_{3/2})$, is given by the RS coupling value, Eq. (4). This can be evaluated using either the free electron g-factor for g_S or, as suggested in Ref. [7], the ground state g-factor $g_J(6^2S_{1/2})$ in Eq. (14) since, according to Eq. (4), the two should be identical.

$$g_J(6^2P_{3/2})_{g_S=g(e)} = 1.334\,103\,68, \qquad (16)$$

$$g_J(6^2P_{3/2})_{g_S=g_J(6^2S_{1/2})} = 1.334\,177\,33. \qquad (17)$$

It should be noted that Eq. (15) is consistent with both Eq. (16) and (17).

Using Eqs. (14) and (15) in Eq. (10), we find

$$\gamma_1 = 13.9925(63) \text{ GHz/T}, \qquad (18)$$

which is the current best value for γ_1.

A theoretical value for the quadratic shift is given by the HCCM value in Eq. (6). Using the effective principal quantum numbers n^* of Ref. [36], we obtain a quadratic shift ξ^{dia}/h of 0.3202 MHz/T^2 for the ground state and 0.7602 MHz/T^2 for the excited state, resulting in an expected diamagnetic shift coefficient of

$$\gamma_2 = 0.4400 \text{ MHz/T}^2. \qquad (19)$$

V. METHOD

A. Realizing saturated absorption spectroscopy inside an MRI scanner

In order to perform saturated absorption spectroscopy inside an MRI scanner, we have developed a nonmetallic fiber-coupled probe containing all the necessary optics shown in Fig. 3. The probe light is delivered to the probe in a single-mode polarization maintaining (PM) fiber and
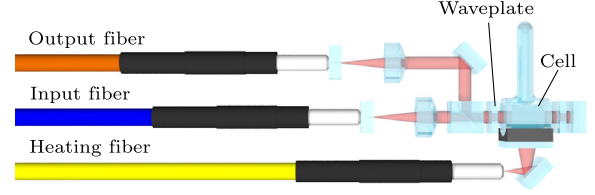

FIG. 3. Optics for performing saturated absorption spectroscopy. The probe light enters through the blue PM fiber and exits through the orange MM fiber. A high-power laser beam delivered through the yellow MM fiber heats the vapor cell. The angle of the quarter-wave plate defines the handedness of the circularly polarized probe light.

returned for detection through a multimode (MM) fiber. To keep the probe and the probed volume small, the optical path length in the cesium vapor cell is only 5 mm, so in order to increase absorption, the cell is heated with a high-power laser beam, delivered through a MM fiber. The fibers are 19 m long.

All optical elements of the probe are mounted in a $90 \times 33 \times 10 \text{ mm}^3$ 3D printed nylon enclosure. A total of five probes have been assembled, as shown in Fig. 4. The quarter-wave plate can be turned 90° to shift the handedness of the circular polarization. For details on the probe design, see Appendix A.

The magnetic susceptibility of the components that make up the probes has been measured, and the associated magnetic field shift at the position of the probing laser beam inside the vapor cell is determined to be

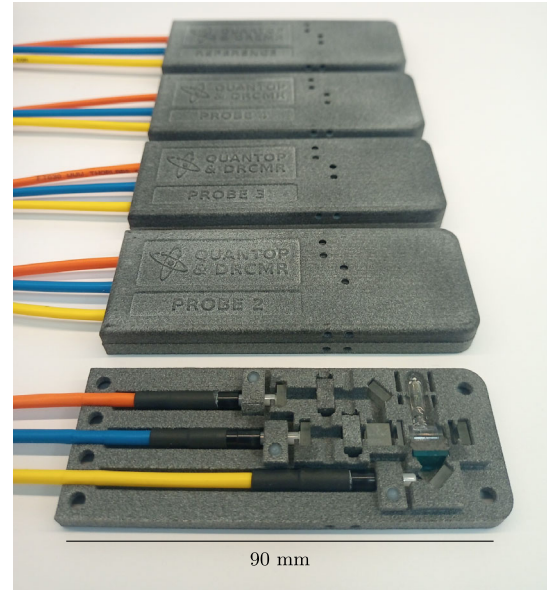$$\zeta = 1 + 0.92(50) \times 10^{-6}. \qquad (20)$$

FIG. 4. Physical realization of the five probes. The cover is removed from probe 1 to show the optics inside.

For details on these measurements and calculations, see Appendix B.

B. Proton spectroscopy

We can accurately measure the magnetic field inside the MRI scanners (Philips Achieva 3 T and 7 T systems) by proton NMR spectroscopy. Using the hardware of the scanner, we excite hydrogen nuclei, in a spherical container of ultrapure water, with an rf pulse and read out the precession frequency ν_p inductively. The magnetic field can then be calculated as

$$B = \frac{\nu_p}{\gamma'_p(t)}, \qquad (21)$$

where $\gamma'_p(t)$ is the shielded proton gyromagnetic ratio corrected for a small dependence on the temperature t. For further details, see Appendix C. We find the field homogeneity to be on the level of 0.3 ppm over the relevant volume.

C. Sideband spectroscopy

Four of the probes are placed in the magnetic field in the center of the MRI scanner, and the fifth is placed in a magnetic shield far away from the MRI scanner. This zero-field reference probe is designed with the quarter-wave plate placed after (instead of before) the cell, such that the probe light polarization is linear. In this way, all the different $|4, m_F\rangle \leftrightarrow |5, m'_F\rangle$ transitions, which are degenerate at 0 T, contribute to the observed line, which will only broaden in a small residual magnetic field rather than shift. We call this line the 0 T transition, and it marks the frequency from where the shifts $\Delta\nu_\pm$ in Eq. (13) are measured. For the four probes inside the MRI scanner, the light is phase modulated by a high-power, high-frequency electro-optic modulator (EOM), generating multiple strong sidebands, below and above the carrier frequency. Two of the probes inside the magnetic field are configured with σ_+ polarization, and two are configured with σ_- polarization. Varying the EOM drive frequency, we can overlap saturated absorption resonances from carrier and sidebands when scanning the laser frequency and thus measure resonance frequency differences as multiples of the EOM drive frequency. The $\pm$5th sidebands are used at 7 T, and the $\pm$3rd sidebands are used at 3 T. This overlap method drastically reduces the sensitivity to nonlinearities of the laser frequency scan. In principle, only one σ_+ and one σ_- configured probe are needed inside the MRI scanner, but the redundancy with four probes enables powerful checks for systematic errors. We use a Toptica DL Pro, 852 nm external cavity diode laser (ECDL) as our probe light source; and a 20 GHz iXblue, high-power, lithium niobate phase modulator as our EOM. The setup is shown in Fig. 5. For further details on the resonance overlapping method, see Appendix D.
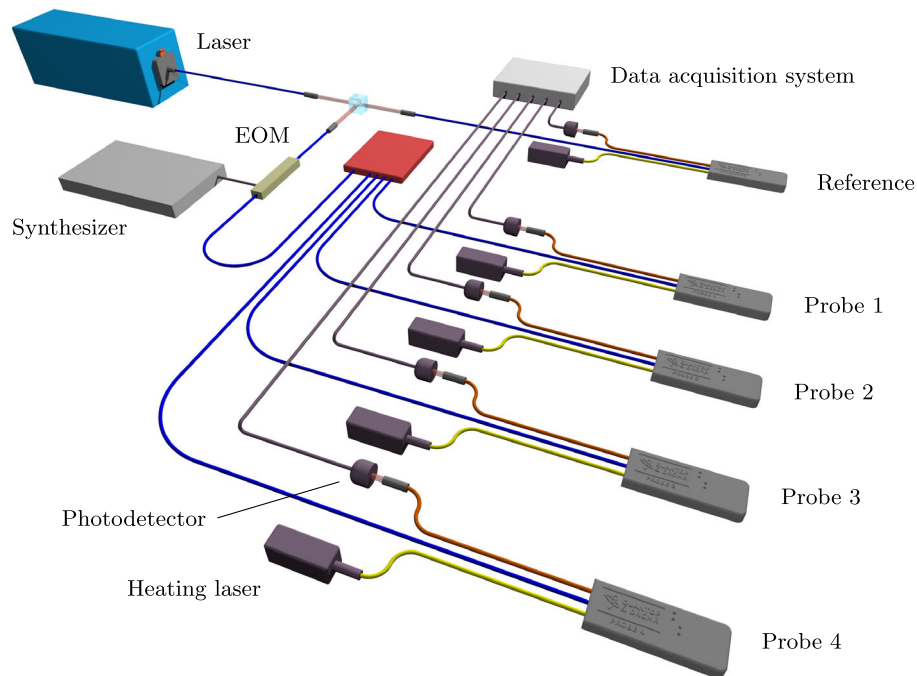

FIG. 5. Optical setup. A laser beam is split into two: One part is sent to the reference probe, which is put inside a magnetic shield. The other part is passed through an EOM, split into four, and sent to each of the four probes, which are located inside the MRI scanner.

D. Data acquisition procedure

A data series is acquired through the following steps:

(i) The water temperature t_a is noted, and proton NMR spectroscopy is performed on the spherical water sample to measure a precession frequency $\nu_{p,a}$.

(ii) The four probes are placed in the MRI scanner instead of the water sample.

(iii) The frequency difference between the extreme σ_+ transition and the extreme σ_- transition, $\Delta\nu_+ - \Delta\nu_-$, is measured by sideband spectroscopy.

(iv) The frequency difference between the extreme σ_+ transition and the 0 T transition, $\Delta\nu_+$, is measured.

(v) The frequency difference between the 0 T transition and the extreme σ_- transition, $-\Delta\nu_-$, is measured.

(vi) Finally, the water temperature t_b is noted, and the water sample is again placed in the MRI scanner, instead of the probes, to measure a precession frequency $\nu_{p,b}$.

The MRI scanner clock ν_c, which is also used as the reference clock for the synthesizer driving the EOM, is continuously monitored throughout the experiment and measured in absolute terms.

A full data acquisition run takes about 45 minutes. For details on how the probes are positioned inside the scanner, see Appendix A.

VI. RESULTS

With the probes positioned in the center of the 7 T MRI scanner, the reference at 0 T, and the EOM driven at $\nu_{EOM} = 19\,592.24$ MHz, we see the three different spectra in Fig. 6. The 0 T spectrum, probed by the carrier frequency, shows the hyperfine structure of the D_2 line; and the two 7 T spectra, simultaneously probed by the ± 5th sidebands, with $\sigma_\pm$ polarization, show the eight transitions with ground state $m_J = \pm\frac{1}{2}$, excited state $m'_J = \pm\frac{3}{2}$, and $m_I = m'_I$ from $\pm\frac{7}{2}$ to $\mp\frac{7}{2}$, from left to right. The extreme $\sigma_\pm$ transitions are the leftmost ones, cf. Fig. 2. Notice how the

extreme $\sigma_\pm$ transitions overlap well with this choice of ν_{EOM}, indicating that the difference $\Delta\nu_+ - \Delta\nu_-$ is about $10 \times \nu_{EOM}$ since this is the frequency difference between the ± 5th sidebands. If no diamagnetic shift exists, these two transitions should also overlap with the 0 T transition probed by the carrier. This is clearly not the case, as they are seen to be about 0.44 MHz/T$^2 \times$ (7 T)$^2 = 22$ MHz higher, as predicted by Eq. (19). The laser frequency is scanned by varying the ECDL control parameters. The frequency axis is determined from knowledge of the 0 T D$_2$ line hyperfine structure, assuming a linear frequency scan.

To obtain an accurate, reproducible, unbiased measurement of the ν_{EOM} that best overlaps the resonances, and hence $\Delta\nu_+ - \Delta\nu_-$, ν_{EOM} is varied and line positions are fitted. The procedure, considered error sources, and associated uncertainty estimates are described in Appendixes D and E.

Six experimental runs are performed. The first two are performed at the 3 T scanner: First, probes 1 and 2 are configured with σ_- polarization, and probes 3 and 4 are configured with σ_+ polarization; second, the opposite configuration is used. Next, the same two configurations are used at the 7 T scanner. Finally, the vapor cells in probe 4 and the reference probe are interchanged, and the same two configurations are used again.

For each experimental run, a line of data is listed in Table II. The data, tabulated chronologically, are acquired from April 17 to May 22, 2022.

A. Calculating the linear magnetic frequency shift

By measuring the frequency difference $\Delta\nu_+ - \Delta\nu_-$, we can eliminate the measurement offset and the quadratic contribution in Eq. (13) to find

$$\Delta\nu_+ - \Delta\nu_- = 2\gamma_1\zeta B. \qquad (22)$$
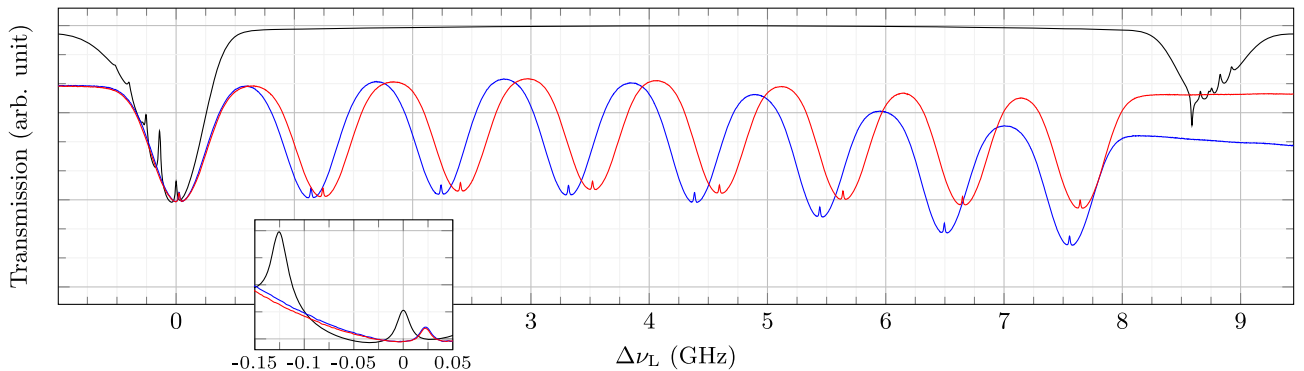
Isolating γ_1 and using Eq. (21), we find

FIG. 6. Scan of the laser frequency over the 0 T spectrum (black line) and the two 7 T spectra as probed by the ± 5th sidebands for $\nu_{EOM} = 19\,592.24$ MHz (the blue line is the σ_+ polarization, and the red line is the σ_- polarization). The laser frequency is shown as a difference $\Delta\nu_L$ from the 0 T transition. Narrow saturation peaks are seen on top of the Doppler broadened lines. The offset between the 0 T transition at 0 GHz and the overlapping extreme $\sigma_\pm$ transitions visible in the inset is due to a diamagnetic shift of about 22 MHz.

TABLE II. Data points underlying the analysis in this work. The configuration refers to the $\sigma_\pm$ polarization of probes 1, 2, 3, and 4, respectively. The asterisk indicates that the cells in probe 4 and the reference have been interchanged. The temperature t is measured next to the water sample just prior to the proton spectroscopy. The proton precession frequency ν_p is determined by NMR spectroscopy. Subscripts a and b refer to measurements before and after the optical measurements, respectively. The optical frequency differences are determined by the overlapping method described in Appendix D. The "10 MHz" MRI scanner clock frequency ν_c, also used as the reference clock for the synthesizer driving the EOM, is measured for each data series.

B	Configuration	t_a (°C)	t_b (°C)	$\nu_{p,a}$ (Hz)	$\nu_{p,b}$ (Hz)	$\Delta\nu_+ - \Delta\nu_-$ (MHz)	$\Delta\nu_+$ (MHz)	$-\Delta\nu_-$ (MHz)	ν_c (Hz)
3 T	$--++$	20.3(5)	20.5(5)	127 778 093(36)	127 778 102(38)	83 998.043(88)	42 003.342(88)	41 994.668(88)	9 999 991(5)
3 T	$++--$	20.0(5)	20.1(5)	127 777 873(32)	127 777 902(41)	83 997.954(88)	42 003.311(88)	41 994.620(88)	9 999 990(5)
7 T	$++--$	20.0(5)	20.0(5)	298 037 732(60)	298 037 734(61)	195 922.431(88)	97 984.127(88)	97 938.342(88)	9 999 992(2)
7 T	$--++$	20.0(5)	20.0(5)	298 037 724(42)	298 037 723(65)	195 922.346(88)	97 984.094(88)	97 938.225(88)	9 999 992(2)
7 T	$--++^*$	20.0(5)	19.9(5)	298 037 732(74)	298 037 732(72)	195 922.303(88)	97 984.058(88)	97 938.256(88)	9 999 992(2)
7 T	$++--^*$	19.4(5)	19.4(5)	298 037 716(62)	298 037 720(61)	195 922.427(88)	97 984.168(88)	97 938.313(88)	9 999 992(2)

$$\gamma_1 = \frac{\Delta\nu_+ - \Delta\nu_-}{2\zeta B}$$
$$= \frac{(\Delta\nu_+ - \Delta\nu_-) \cdot \gamma'_p(t)}{2\zeta\nu_p}. \tag{23}$$

Notice that this expression contains the ratio of two frequency measurements: the proton precession frequency and the optical frequency difference. This means that it is not sensitive to the absolute accuracy of these frequencies, as long as a single common clock is used, as is the case for our experiment.

For each line in Table II, two values for γ_1 are calculated: one based on the single direct measurement of the optical frequency difference $\Delta\nu_+ - \Delta\nu_-$, and one based on the sum of the two measurements $\Delta\nu_+$ and $-\Delta\nu_-$. The proton precession frequency for each line is taken to be the average of the measurement before and after, with the uncertainty taken to be the difference, plus the two individual uncertainties, and similarly for the temperature, except that we only include the thermometer uncertainty of 0.5 °C once. The resulting values are displayed in Table III, along with the MRI scanner magnetic field and the probe polarization configuration. We find the mean of these values to be

$$\gamma_1 = 13.994\,301(11) \text{ GHz/T}. \tag{24}$$

TABLE III. Different determinations of γ_1. The values in the third column are calculated using the single measurement $\Delta\nu_+ - \Delta\nu_-$. The values in the fourth column are calculated using the sum of the measurements $\Delta\nu_+$ and $-\Delta\nu_-$.

B	Configuration	γ_1 (GHz/T) (single)	γ_1 (GHz/T) (sum)
3 T	$--++$	13.994 299(19)	13.994 294(24)
3 T	$++--$	13.994 308(20)	13.994 304(25)
7 T	$++--$	13.994 304(11)	13.994 307(13)
7 T	$--++$	13.994 299(11)	13.994 297(12)
7 T	$--++^*$	13.994 295(12)	13.994 296(13)
7 T	$++--^*$	13.994 305(11)	13.994 309(13)

For the uncertainty, we simply take the lowest of the uncertainties from Table III, recognizing that part of the uncertainty comes from the probe field shift ζ and is common to all the measurements, and other systematic error sources might also be at work. The value in Eq. (24) represents an improvement in accuracy of more than 2 orders of magnitude compared to Eq. (18). The data in Table III are shown in Fig. 7. All reported uncertainties in this work should be interpreted as 1 standard deviation.

B. Calculating the Landé g-factor for the excited state

Isolating $g_J(6^2P_{3/2})$ in Eq. (10) and using the result in Eq. (24), we find

$$g_J(6^2P_{3/2}) = \gamma_1 \cdot \frac{2h}{3\mu_B} + \frac{g_J(6^2S_{1/2})}{3}$$
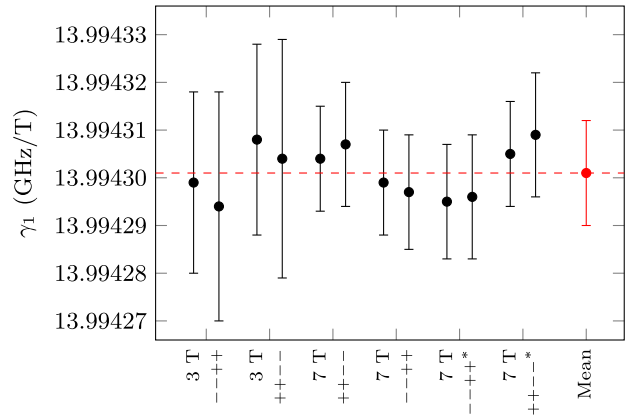$$= 1.334\,087\,49(52), \tag{25}$$

FIG. 7. Values for γ_1 from Table III (black), along with the mean value (red). Error bars, which include estimates of systematic errors, are obtained as described in the text and should be interpreted as 1 standard deviation.
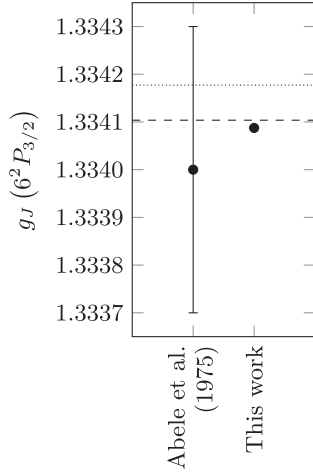
FIG. 8. Comparison of our result, Eq. (25), with the best previous measurement [38], and the two RS values. The dashed line represents the RS value calculated using the free electron g-factor as g_S, Eq. (16). The dotted line represents the RS value calculated using the ground state g-factor as g_S, Eq. (17). The uncertainty on our result is too small to be shown as an error bar in this plot. The error bar on the result from Ref. [38] is described as including "possible systematic errors as well as three times the standard deviation."

which can be compared to the previous best value, Eq. (15), measured by Abele *et al.* (1975) [38], and the RS values, Eqs. (16) and (17), in Fig. 8. As with the γ_1 measurement, we see an improvement in accuracy of more than 2 orders of magnitude. The RS value calculated using the free electron g-factor as g_S, Eq. (16), is the prediction closest to our result. However, the discrepancy is 31 standard deviations and hence substantial.

C. Determining the frequency shift measurement offset

To determine the measurement offset γ_0, we reorganize Eq. (13) to read

$$\Delta\nu_\pm \mp \gamma_1\zeta B = \gamma_0 + \gamma_2\zeta^2 B^2. \tag{26}$$

For each line in Table II, a magnetic field B is calculated using Eq. (21), and the left-hand side is calculated for the values $\Delta\nu_\pm$ using the result in Eq. (24) for γ_1. This data set is fitted, without taking uncertainties into account, with the quadratic right-hand side, as shown in Fig. 9, to produce the value

$$\gamma_0 = 0.159(159) \text{ MHz}. \tag{27}$$

Since this number should be zero and we do not know exactly the cause of this deviation, we take the uncertainty to be 100%, even though the largest residual from the fit is 0.069 MHz. We note that this measurement offset is small
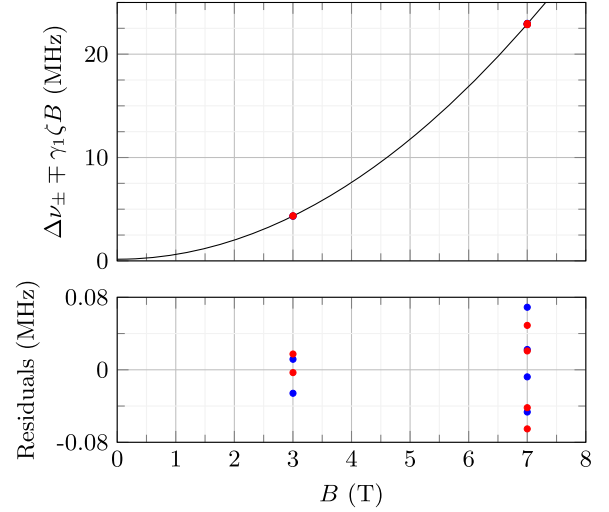

FIG. 9. Data $\Delta\nu_\pm \mp \gamma_1\zeta B$, fit $\gamma_0 + \gamma_2\zeta^2 B^2$, and residuals. Blue data are from the σ_+ configured probes, and red data are from the σ_- configured probes. The least-squares fit produces the values $\gamma_0 = 0.159$ MHz and $\gamma_2 = 0.4644$ MHz/T^2. This method is only used to estimate γ_0 and not γ_2 since it does not provide a good estimate for the uncertainty.

compared to the linewidth of the transition, as expected. Here, the clock inaccuracy, listed in Table II as ν_c, is taken into account but is found to be negligible.

It should be stressed that γ_0 is an experimental offset that depends on the physical implementation of the measurement. We report it here since it gives a good estimate of the accuracy of the method and because we need it for the calculations in the next section.

D. Calculating the quadratic diamagnetic shift

By measuring, and adding, the optical frequency shifts $\Delta\nu_+$ and $\Delta\nu_-$, we can eliminate the linear part in Eq. (13) to obtain

$$\Delta\nu_+ + \Delta\nu_- = 2\gamma_0 + 2\gamma_2\zeta^2 B^2. \tag{28}$$

Isolating γ_2 and using Eq. (21), we find

TABLE IV. Different determinations of γ_2. Also shown are the values γ_2^d, directly calculated without taking the measurement offset γ_0 into account.

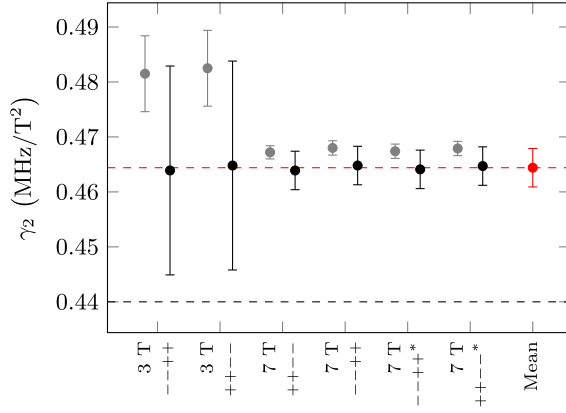| B	Configuration	γ_2 (MHz/T^2)	γ_2^d (MHz/T^2)
3 T	$--++$	0.4639(190)	0.4815(69)
3 T	$++--$	0.4648(190)	0.4825(69)
7 T	$++--$	0.4639(35)	0.4672(13)
7 T	$--++$	0.4648(35)	0.4680(13)
7 T	$--++^*$	0.4641(35)	0.4674(13)
7 T	$++--^*$	0.4647(35)	0.4679(13)

FIG. 10. Values for γ_2 from Table IV (black), along with the mean value (red). The direct calculations γ_2^d, not taking the experimental offset γ_0 into account, are shown in gray. The dashed black line shows the HCCM value from Eq. (19). Error bars, which include estimates of systematic errors, are obtained as described in the text and should be interpreted as 1 standard deviation.

$$\gamma_2 = \frac{\Delta\nu_+ + \Delta\nu_- - 2\gamma_0}{2\zeta^2 B^2}$$
$$= \frac{(\Delta\nu_+ + \Delta\nu_- - 2\gamma_0) \cdot (\gamma_p'(t))^2}{2\zeta^2 \nu_p^2}. \qquad (29)$$

Notice that this expression *is* sensitive to the absolute accuracy of the clock, unlike Eq. (23). The (in this case, insignificant) frequency correction is made by multiplying the denominator by a factor $\nu_c \times (10 \text{ MHz})^{-1}$.

For each line in Table II, a value for γ_2 is calculated. The resulting values are displayed in Table IV, along with the MRI scanner magnetic field and the probe polarization configuration. We find the mean of these values to be

$$\gamma_2 = 0.4644(35) \text{ MHz/T}^2. \qquad (30)$$

For the uncertainty, we simply take the lowest of the uncertainties from Table IV, as in Eq. (24). Also shown in Table IV are values γ_2^d directly calculated, without taking the measurement offset γ_0 into account. The data in Table IV are shown in Fig. 10. Since these are the first such measurements, we do not have any other experimental data to compare them to. We notice that the mean value in Eq. (30) is on the same order of magnitude as the HCCM value found in Eq. (19) (also shown in Fig. 10), however, with a significant discrepancy of 7 standard deviations.

VII. CONCLUSION

In this work, we have investigated the cesium D_2 transitions involving the extreme angular-momentum states. The magnetic field dependence of these transitions has been mapped with unprecedented accuracy compared

to any other alkali optical transition, enabling accurate optical magnetometry at high magnetic fields.

It is very interesting to note that the excited state g-factor calculated in Eq. (25) is not in agreement with the RS coupling value of Eq. (16), as we find a discrepancy of -1.6×10^{-5}, significant to 31 standard deviations. According to Ref. [29], until now, all measurements on alkali non-S states have been in agreement with the RS value. For D states in cesium, discrepancies up to -5.5×10^{-5} are predicted theoretically using more advanced methods [39]. No theoretical predictions have been published yet for the P states.

It is also very interesting to note that the quadratic diamagnetic shift is not in agreement with the HCCM value. Most of the data presented in Ref. [35] show very good agreement with the HCCM value; only for potassium are discrepancies of up to 2.7 standard deviations reported. Here, we report a highly significant discrepancy of 7 standard deviations.

These results could motivate theoretical work on high-accuracy calculations beyond the RS coupling scheme and the HCCM assumption.

VIII. OUTLOOK

It should be noted that similar measurements can be made for other transitions and other alkali atoms. This could enable high-accuracy magnetometry with other laser wavelengths or other alkali atoms, and provide more data for testing of atomic structure models. In future studies, possibly involving many different magnetic fields, the possibility of the simple model described by Eq. (13) being insufficient should also be considered. This may become relevant for very accurate measurements or very high fields. For a discussion of possible future improvements to this kind of experiment, see Appendix F.

We are currently working to develop the system presented in this work into a fully functional high-speed magnetometer by implementing continuous tracking of the magnetic frequency shift $\Delta\nu_+$ in Eq. (13). Such a magnetometer could have applications in MRI, as described in Ref. [41], as well as other areas where high magnetic fields need to be stabilized or monitored. For a discussion on measurement strategies, see Appendix G.

The data sets and scripts for the analysis and calculations underlying this work are openly available from Ref. [40].

APPENDIX A: PROBE DESIGN

The MRI-compatible fiber-coupled probe design is shown in Fig. 11. After the 852 nm probe light emerges from the blue PM fiber, with an angle of 4.9°, the beam is collimated by a lens, with a focal length $f = 10$ mm, to have a waist of 0.86 mm. After passing through the polarizing beam splitter (PBS), the quarter-wave plate,
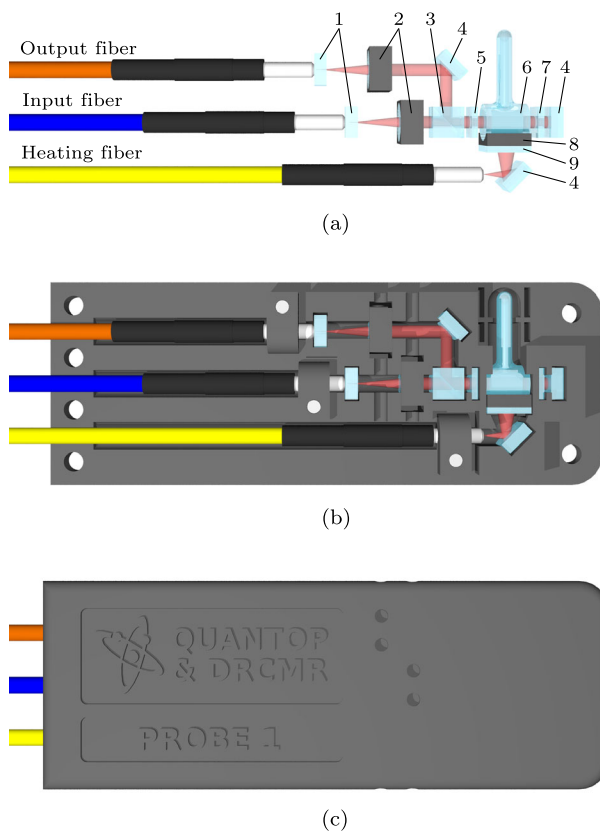
(a)

(b)

(c)

FIG. 11. Optical elements of the probe and how they are mounted inside the nylon holder. (a) 1: AR coated windows. 2: Lenses glued into cubic nylon holders. 3: PBS. 4: Mirrors. 5: Quarter-wave plate. 6: Vapor cell. 7: Optical filter with 40% transmission at 852 nm. 8: Heat conducting silicone. 9: Optical filter with 1.2% transmission at 808 nm. (b) The whole setup is put in a nylon holder. Mirrors, PBS, and windows are glued in. The fibers are clamped by the ceramic ferrules, with nylon bolts from below. Lens holders are fitted tightly into theirs slots. (c) A protective cover is fastened on top of the holder with nylon bolts from the bottom. Lens positions can be adjusted by pushing through the holes from the outside.

and the vapor cell, the beam is cut by an aperture of 2 mm diameter. This means that the measurement volume of the probe is bounded by a cylinder of 2 mm diameter and 5 mm length. The return beam intensity is attenuated to 16% by passing an optical filter twice to avoid excessive power broadening of the saturated absorption signal. Another $f = 10$ mm lens focuses the beam into a MM fiber with a core diameter of 0.4 mm. The 808 nm heating laser light is delivered through a similar MM fiber. The heating laser beam is absorbed in an optical filter, and a silicone heat conductor transfers the heat to the vapor cell, allowing for very localized heating. With the stem of the vapor cell pointing away from the point of heating, it is ensured that the coldest point of the cell is far away from the probing beam path, such that cesium does not condense on the windows and block the probe beam. The two probe-beam input and output fibers are terminated by windows with antireflection (AR) coating on the side facing away from the fibers to reduce spurious etalon fringes from the fibers in the spectrum. Index matching gel is applied at the interface between the fiber tips and the windows. The fibers are 19 m long. Mirrors, windows, and PBS are fastened with glue. The lenses are glued into cubic holders, which are mounted by a tight fit in their slots.

The nylon enclosure measures $90 \times 33 \times 10$ mm³ and is 3D printed using HP Multi Jet Fusion (MJF) technology. While stereolithographic (SLA) 3D printing produces very nice results, as demonstrated in Ref. [42], the material is not compatible with temperatures approaching $100\,°C$, like nylon, which is why the MJF method is used here.

By pushing through holes from the outside, the lens positions can be adjusted to optimize the beam direction and output fiber coupling. We achieve a fiber coupling close to 100%, reasonably stable during daily handling.

During the experiments described in this work, the four probes are strapped together by two thin sewing threads, in a configuration with probes 2 and 4 on top of probes 1 and 3, as shown in Fig. 12. When the spherical water sample is removed from the MRI scanner during a data acquisition
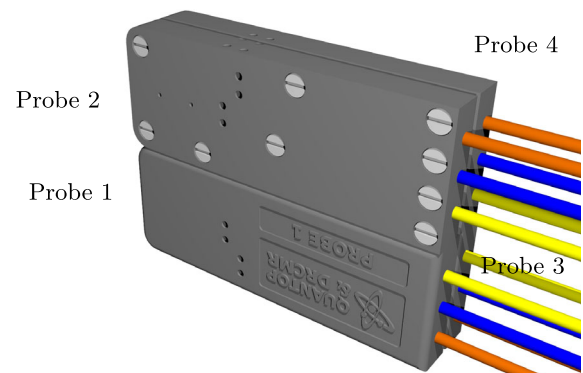
FIG. 12. The four probes in the configuration used inside the scanner. The probes are held together by two thin sewing threads (not shown in the image). The field direction is parallel to the fibers.

run, the probes are positioned, as well as possible, at the center of where the sample used to be, pointing along the field direction, suspended from a thin sewing thread. The sewing threads are assumed to have a negligible effect on the magnetic field.

It should be noted that small angular misalignments of the probes and imperfect polarizing optics will only lead to small reductions in the signal—not frequency shifts—since the frequency shifts are only sensitive to the magnitude of the magnetic field.

Probes 1 and 3 are heated with 600 mW of optical power, and probes 2 and 4 are heated with 500 mW. The reference probe is heated with 250 mW. After about an hour, the probe temperatures stabilize around 43 °C, and the reference temperature stabilizes around 35 °C. This corresponds to a cesium atomic density of about 26×10^{16} m^{-3} for the probes and 13×10^{16} m^{-3} for the reference. Compared to about 3×10^{16} m^{-3} at room temperature, this gives a significant increase in absorption depth and hence signal strength.

About 542 µW of optical probe power is sent to the probes, and about 175 µW is sent to the reference. Notice that for the probes, only a smaller fraction of the probe light is actually resonant, as the sidebands generated by the EOM are the ones used. At 3 T, third sidebands are used, and at 7 T, fifth sidebands are used. This means that only about 19% and 14% of the probe light is on resonance, respectively.

APPENDIX B: MAGNETIC FIELD SHIFT OF THE PROBES

The shielded proton gyromagnetic ratio is defined such that the field that is measured is the one in the vacuum left when the spherical water sample is removed. When the sphere is removed and replaced with the four probes and air, the magnetic field is changed slightly due to the change in magnetic susceptibility. This is taken into account by the factor ζ introduced in Eq. (13). We have measured the volume magnetic susceptibility χ for all the components of

the probes using a method similar to that described in Ref. [43]: A sample of the component material is submerged in water, and the field distortion around the sample is mapped using the 7 T MRI scanner. From a fit, the difference in sample and water magnetic susceptibilities, $\chi - \chi_{H_2O}$, is determined. The sample magnetic susceptibility is then found using $\chi_{H_2O} = -9.0559(61)$ ppm [44]. For components easily isolated, the results are shown in Table V. We note that the values for $\chi - \chi_{H_2O}$ found for Schott Borofloat 33 and Schott N-BK7 agree with the values from Ref. [43] within about 5%. Hence, this is chosen as the level of uncertainty, implying that magnetic susceptibilities close to χ_{H_2O} are measured much more accurately than those far away. Notice how the optical filters are highly paramagnetic, especially the probe beam filter.

For the fiber cables (i.e., the outer jacket of the cable and everything inside it, including air) and the fittings (which keep the fiber cables and the fiber ferrules together), "effective" magnetic susceptibilities are determined for the compound components. The results are shown in Table VI. Since this is measured without disassembling the fiber cables, the method is less accurate. We find the uncertainty to be 25% by comparing the measurement on the zirconia ferrules in the assembled fiber cables to the measurement on pure zirconia. Detailed knowledge of these components is fortunately not important for the field shift at the position of the vapor cell.

For the vapor cell, a model is constructed using the value for quartz glass from Ref. [43] [$\chi = -11.30(1)$ ppm] and vacuum ($\chi = 0$). The field shift of this model is seen to match reasonably well with the measured field shift from a vapor cell. Our vapor cells are made from Momentive GE214 Fused Quartz (body) and Corning 7980 Fused Silica (windows) by Precision Glass Blowing.

The magnetic susceptibility of the surrounding air is taken to be $\chi_{Air} = 0.36$ ppm, as in Ref. [45].

The magnetic susceptibility of cesium is calculated from the data in Ref. [46] to be 5.1 ppm. Hence, the very small amounts of cesium sitting in the bottom of the vapor cell stem can safely be ignored. Similarly, the glue used to hold

TABLE V. Volume magnetic susceptibility measurements on parts consisting of only a single material. The method is estimated to be accurate to about 5% for the value of $\chi - \chi_{H_2O}$.

Material	Component	$\chi - \chi_{H_2O}$ (ppm)	χ (ppm)
Unknown	Heating beam filter	18.47(92)	9.41(92)
MJF Nylon PA12	3D print	0.1209(60)	−8.9350(86)
Nylon 66 UL94V-2	Bolts	−0.213(11)	−9.269(13)
Synthetic quartz	Quarter-wave plate	−4.34(22)	−13.39(22)
Schott Borofloat 33	Mirrors and windows	−2.13(11)	−11.19(11)
Schott N-BK7	Lenses	−3.31(17)	−12.37(17)
Schott N-SF1	PBS	−0.524(26)	−9.580(27)
Schott NG4	Probe beam filter	149.3(75)	140.2(75)
Silicone, RS 174-5694	Heat conductor	−1.273(64)	−10.329(64)
Zirconia	Fiber ferrules	−1.053(53)	−10.109(53)

TABLE VI.   Volume magnetic susceptibility measurements on compound parts not easily separated in single materials. The method is estimated to be accurate to about 25% for the value of $\chi - \chi_{H_2O}$.

Component	$\chi - \chi_{H_2O}$ (ppm)	χ (ppm)
Fiber cable (heat)	1.38(34)	−7.68(34)
Fiber cable (in)	2.45(61)	−6.61(61)
Fiber cable (out)	1.12(28)	−7.93(28)
Fitting (heat)	4.6(12)	−4.4(12)
Fitting (in)	2.21(55)	−6.84(55)
Fitting (out)	4.6(11)	−4.5(11)

FIG. 15.   Distribution of voxels in the beam path inside the vapor cell according to the simulated field shift. Notice how the highly paramagnetic optical filter next to the vapor cell creates a magnetic field gradient along the beam path.

the optical elements in place, the index matching gel, and the thin optical coatings are assumed to be negligible.

Using all the above, a 3D susceptibility model of the probe is constructed, as seen in Fig. 13. Using the method described in Refs. [47,48], we then calculate the field shift caused by this distribution of magnetic susceptibility. This method takes into account the effect of the Lorentz sphere, i.e., the effect of the granular structure of matter [49,50]. Since we are concerned with the field shift in the vacuum inside the vapor cell, we find the "continuous-matter field shift" by adding $\frac{2}{3}\chi$ to the calculated field shift. Since the calculation is performed on the susceptibility relative to the surrounding air, we also add $\frac{2}{3}\chi_{Air}$ to account for the sphere of air that replaces the sphere of water. The resulting field shift map is shown in Fig. 14. It should be noted that including the Lorentz sphere also works since, in this case, there is no field shift from the sphere of air that surrounds the probe.

FIG. 13.   Cross section of the 3D susceptibility model of the probe. The cross section is made through the center of the vapor cell. We cap the color scale at 20 ppm, even though the probe filter susceptibility is 140 ppm, to highlight the details of the entire structure.
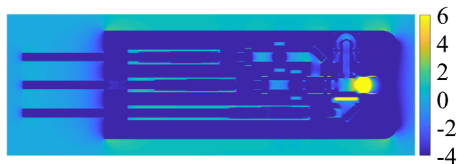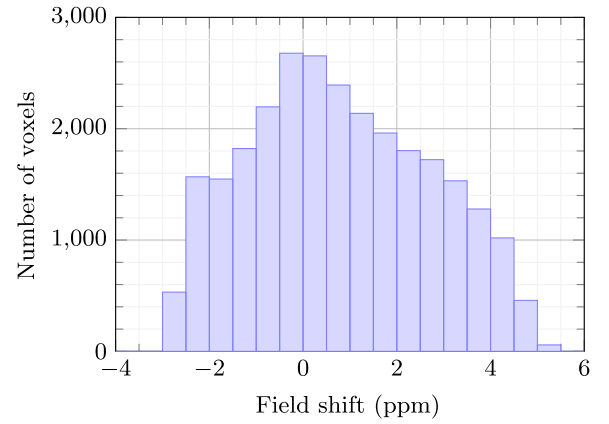

FIG. 14.   Calculated field-shift map. The cross section is the same as in Fig. 13. The effect of the rest of the fibers, not included in this model, is verified through a similar simulation to have a negligible effect at the position of the vapor cell. We cap the color scale to match the distribution inside the vapor cell.

Picking out the voxels that make up the probe beam path inside the vapor cell, we find a distribution of field shifts as seen in Fig. 15. By varying the voxel size, the surrounding zero padding, the magnetic susceptibilities of components close to the vapor cell, and the exact position of the highly paramagnetic probe filter, we find the mean value for the field shift in the beam path inside the vapor cell to be $1 + 0.49(50) \times 10^{-6}$. The uncertainty on this number also takes into account the variation over the radius of the beam since it is not clear if the center or the edge of the beam contributes the most to the measured signal. The main contribution to the uncertainty is related to the uncertainty on the probe filter susceptibility and its exact position. A similar calculation is performed on a model of all four probes strapped together, as seen in Fig. 12, to give

$$\zeta = 1 + 0.92(50) \times 10^{-6}. \qquad (B1)$$

APPENDIX C: MAGNETIC FIELD DETERMINATION BY PROTON NMR SPECTROSCOPY

Accurate magnetic field determinations in the tesla range, uses that the shielded proton gyromagnetic ratio is known with very high accuracy [16,28,44] as

$$\gamma_p'(25\,°C) = 42.576\,384\,74(46) \text{ MHz/T}. \qquad (C1)$$

This value refers to hydrogen nuclei (protons) in a spherical sample of pure water at $25\,°C$. The water shielding factor depends slightly on the temperature t [44,51] as

$$\frac{\gamma_p'(t)}{\gamma_p'(25\,°C)} = 1 - 10.36(30) \times 10^{-9}\,°C^{-1}(t - 25\,°C). \qquad (C2)$$

TABLE VII. Downmixing ν_0 and peak frequencies ν_m for the six data acquisition runs. Subscripts a and b refer to measurements before and after the optical measurements, respectively.

B	Configuration	ν_0 (Hz)	$\nu_{m,a}$ (Hz)	$\nu_{m,b}$ (Hz)
3 T	$--++$	127 778 089	4(36)	13(38)
3 T	$++--$	127 777 868	5(32)	34(41)
7 T	$++--$	298 037 729	3(60)	5(61)
7 T	$--++$	298 037 737	$-13(42)$	$-14(65)$
7 T	$--++^*$	298 037 744	$-12(74)$	$-12(72)$
7 T	$++--^*$	298 037 724	$-8(62)$	$-4(61)$

Using nuclear rf excitation and subsequent readout of the free induction decay (FID), the proton precession frequency ν_p is measured. The magnetic field can then be found as

$$B = \frac{\nu_p}{\gamma'_p(t)}. \tag{C3}$$

The magnetic field B is defined as the field in the vacuum left when the sphere of water is removed. Notice that the material of the container is not important as the field shift inside a spherical shell is zero [52].

For our case, where we use an MRI scanner, the acquired rf signal is first downmixed by a frequency ν_0, chosen by the scanner, close to the actual resonance frequency. The measured frequency of the FID is then ν_m, such that $\nu_p = \nu_0 + \nu_m$. We find ν_m as the peak value of the Fourier transform of the downmixed FID signal. The uncertainty is estimated by inspection of a field image of the spherical water sample produced by the scanner. For the 3 T scanner, the full width at 25% of the peak value is found to be a good estimate for the uncertainty. For the 7 T scanner, the full width at 5% of the peak value is used. For the six data acquisition runs, we note ν_0 and ν_m in Table VII. The proton precession frequencies in Table II follow. Notice that imperfections in the spherical shape—such as container deformations, residual air bubbles, and the small hole used for water filling—are taken into account by this uncertainty estimation. The sphere has a diameter of 100 mm and hence covers a much larger volume than the four vapor cells.

APPENDIX D: MEASURING OPTICAL FREQUENCY DIFFERENCES

Central to this work is the method to accurately measure a resonance frequency difference by sideband spectroscopy. By choosing an EOM modulation frequency ν_{EOM} equal to an integer fraction of the resonance frequency difference, the saturated absorption peaks as probed by the carrier or sidebands, can be brought to overlap. To do this in a systematic and unbiased way, a series of different frequencies, ν_{EOM}, are tried. In steps of 0.01 MHz, a range

of 0.20 MHz is covered. For each ν_{EOM}, 100 laser frequency scans are averaged. As an example, we take the determination of the difference $\Delta\nu_+ - \Delta\nu_-$ in the last line in Table II, i.e., in the 7 T scanner, with probes 1 and 2 configured with σ_+ polarization and probes 3 and 4 with σ_- polarization. In Fig. 16, we show a laser frequency scan (average of 100) with $\nu_{EOM} = 19\,592.14$ MHz, such that the ± 5th sidebands probe the extreme $\sigma_\pm$ transitions. A fit of a second-degree polynomial background and a Lorentzian line shape is performed for each probe. The frequency axis is estimated in a prior scan across the 0 T spectrum from the reference probe. The exact scaling is not important. Changing ν_{EOM} in steps of 0.01 MHz up to 19 592.34 MHz, we obtain a series of fitted relative line centers as a function of $10 \times \nu_{EOM}$, as shown in Fig. 17. Straight lines are fit to the data, and the four intersections are found. The optical frequency difference is then found as their average to be $\Delta\nu_+ - \Delta\nu_- = 195\,922.427$ MHz. Similarly, the difference $\Delta\nu_+$ is found by sweeping ν_{EOM} across the frequency that overlaps the extreme σ_+ transition as probed by the fifth upper sideband, with the 0 T transition, as probed by the carrier. Here, only two intersections are found since there is only one reference probe. Finally, $-\Delta\nu_-$ is found by overlapping the extreme σ_- transition, as probed by the fifth lower sideband, with the 0 T transition, as probed by the carrier. In these two cases, the frequency difference is found as $5 \times \nu_{EOM}$. For the 3 T measurements, ± 3rd sidebands are used with EOM frequencies of about 14 GHz, and hence frequency differences are found as $6 \times \nu_{EOM}$ and $3 \times \nu_{EOM}$, correspondingly.

To estimate the uncertainty on the overlapping procedure, we note that the first measurement, $\Delta\nu_+ - \Delta\nu_-$, should equal the sum of the measurements $\Delta\nu_+$ and $-\Delta\nu_-$, so the difference between those two numbers represents an
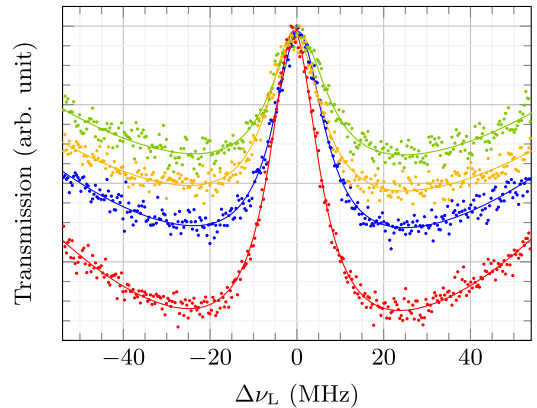

FIG. 16. Average of 100 laser frequency scans with $\nu_{EOM} = 19\,592.14$ MHz. The fifth upper sideband probes the extreme σ_+ transition in probes 1 and 2 (blue and green), and the fifth lower sideband probes the extreme σ_- transition in probes 3 and 4 (yellow and red).
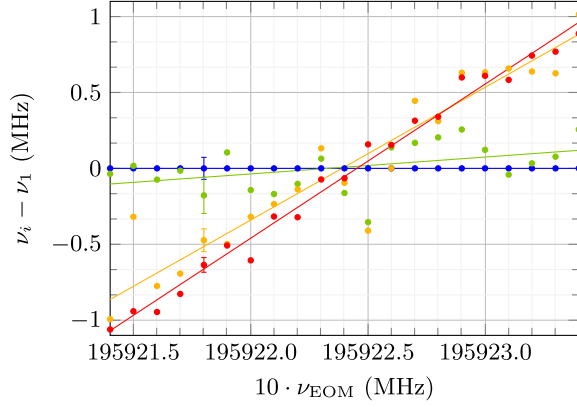
FIG. 17. Line center ν_i for probes $i = \{1, 2, 3, 4\}$ relative to ν_1 as a function of $10 \times \nu_{\mathrm{EOM}}$. Colors are as in Fig. 16. The leftmost data points correspond to the line centers found from the fits in Fig. 16. Error bars are found as 68% confidence intervals, i.e., 1 standard deviation, as detailed in Ref. [53]. To keep the figure clear and readable, error bars are shown only for a single representative line of data.

uncertainty on the overlapping procedure. We find the root mean square of the differences to be 0.034 MHz.

Apart from the overlapping procedure, there is also an uncertainty on how well the fitted line-shape center represents the actual resonance frequency. In particular, a significant "geometrical shift" has been observed, clearly correlating with the geometrical broadening (see, e.g., Ref. [54]) associated with the lenses not being well positioned such that the beam is not reflected exactly 180° backwards through the vapor cell. All lenses are adjusted as well as possible to reduce the geometrical broadening and shift. Configuring all the probes with σ_+ polarization, we see a variation of up to 0.054 MHz between the probes. Any shift common among probes 1–4 but differing from the reference probe is described by the constant γ_0 in Eq. (13).

We add the two above-described error sources to get 0.088 MHz, which is the uncertainty used for the optical frequency differences in Table II. Other considered error sources are discussed in Appendix E.

APPENDIX E: OPTICAL-RESONANCE-SHIFTING ERROR SOURCES

A number of error sources potentially contributing to a systematic shift of the optical resonance frequencies have been considered in this work. Most notably is the geometrical shift associated with lens positions and the related geometrical broadening of the line at 3 T and 7 T. We have not observed a similar shift at 0 T, making this a good candidate for explaining the measurement offset γ_0. With poor lens adjustment, we have observed linewidths up to 30 MHz and line-center shifts up to 0.4 MHz. By proper lens adjustment, linewidths of about 16 MHz are achieved. Apart from power broadening, this may also contain a

residual geometrical broadening common among the probes. Hence, a related geometrical shift of about $\gamma_0 = 0.159$ MHz is very reasonable. An inability of the fit (a second-degree polynomial background and a Lorentzian line shape) to nicely find the line center in the asymmetric 0 T spectrum might also contribute to γ_0. However, with an estimated uncertainty of 100% in γ_0, these error sources are accounted for in our final result for γ_2. Note that the geometrical shift seems to be the same for the extreme σ_+ and σ_- transitions; hence, the probe configuration alternations ($--++ \leftrightarrow ++--$) actually remove this error source in the γ_1 result and the derived Landé g-factor result. Unfortunately, the handling of the probes in between the different measurements might shift the lens positions slightly, so we cannot claim a complete immunity to this shift.

Since the probe and the reference cells are kept at different temperatures, one might also suspect that a pressure shift could contribute to γ_0. However, measurements at both 3 T and 7 T, with the probe cells at room temperature, show no significant shift of the line center compared to the measurements with the probe cells at 43 °C. Pressure shifts with buffer gasses are typically up to about 10 MHz/torr [55]. Since the pressure in our cells is about 10^{-5} torr (i.e., the cesium vapor pressure), we expect pressure shifts of only up to 0.0001 MHz if the results from buffer gasses can be applied to pure cesium.

A significant error source that has been considered is the unavoidable higher-order sidebands probing the more magnetic-field-sensitive transitions with the ground state $m_J = -\frac{1}{2}$ and the excited state $m'_J = +\frac{1}{2}$. In particular, at 7 T, the eighth lower sideband in the σ_- configured probes produces a weak peak that can, in fact, impact the line-center determination. In experiments, this manifests as a clear discrepancy between the first measurement $\Delta\nu_+ - \Delta\nu_-$ and the sum of the measurements $\Delta\nu_+$ and $-\Delta\nu_-$. For our measurements at 7 T, we have therefore turned the EOM drive power down a bit from where the optical power in the fifth sideband is optimized. Thus, the eighth sideband can be greatly reduced while the fifth is only slightly reduced. Still, this error source cannot be completely removed and is hence accounted for through the uncertainty in the peak overlapping procedure.

The light shift (ac Stark effect) from the sidebands, not on resonance but detuned by multiples of ν_{EOM}, will shift the resonant transition slightly. For our case of detunings that are large compared to the Doppler width, the light shift is well approximated by

$$\Delta\nu_{\mathrm{light}} = \frac{\Gamma^2 I/I_{\mathrm{sat}}}{4(2\pi)^2 \delta}, \tag{E1}$$

where Γ is the decay rate of the excited state, I is the light intensity, I_{sat} is the saturation intensity, and δ is the detuning for the sideband under consideration [26,52,56]. This effect

will be strongest for the experiments at 3 T using the third sidebands. In this case, in the center of the beam, we have approximately $I/I_{sat} = 10$ for the sideband *on* resonance. Considering that the two neighboring sidebands are approximately half the intensity, and using $\delta = 14$ GHz, this gives a light shift of about 0.002 MHz. Since the two nearest sidebands in fact shift in opposite directions, we find this effect to be negligible. In addition, we have experimentally investigated the probe power dependence of the line center: At both 3 T and 7 T, we have reduced the probe power by 50% without observing any significant change in the line-center determination. Since a light shift would be proportional to the probe power, we conclude that this error source is indeed negligible.

As shown in Ref. [57], the pressure of the probe light exerts a force on the atoms that breaks the symmetry of the velocity distribution. We have not considered this effect in detail but note that it might contribute to γ_0. In fact, it may actually contribute to what we here call a geometrical shift.

APPENDIX F: FUTURE HIGH-ACCURACY MEASUREMENTS

To improve on the experiments presented in this work, a number of steps can be taken:

(i) Increasing the magnetic field will be useful, in particular, for measuring the quadratic diamagnetic shift. MRI systems, NMR spectrometers, or custom-made systems may be employed. As shown here, it can be useful to include more than one magnetic field in a study when measuring the quadratic shift, whereas the linear shift can reliably be measured using only a single magnetic field.

(ii) Improving on the field homogeneity (shimming) will be necessary to gain the most from using higher magnetic fields.

(iii) Using higher EOM drive frequencies, such that lower-order sidebands are employed, could provide a better signal-to-noise ratio and remove the problem of higher-order sidebands probing higher-lying transitions.

(iv) Developing a more robust probe design—which can sustain higher cell temperatures, has fixed and well-overlapping beams, and does not include highly paramagnetic components that complicate magnetic-field-shift calculations—could also make future measurements more accurate and possibly reduce γ_0.

(v) Alternatively, one could employ a spherical vapor cell that simply replaces the spherical water container in the setup, similarly to the approach taken in the measurement of the shielded proton gyromagnetic ratio [16]. This would remove the error source introduced by the probe field shift.

APPENDIX G: HIGH-FIELD OPTICAL MAGNETOMETRY

Here, we consider two measurement methods to implement high-field optical magnetometry.

The first method involves measuring the frequency shift from the resonance at 0 T to the resonance in field B. This method uses a single reference probe and any number of probes in the magnetic field, depending on the spatial resolution needed for the application. The laser frequency can be stabilized using the reference, while EOM generated sidebands are used to track the resonances from the probes in the magnetic field. Assuming that σ_+ configured probes are used, the magnetic field is calculated from the frequency shift, using Eq. (13), as

$$B = \frac{-\gamma_1 + \sqrt{\gamma_1^2 - 4\gamma_2(\gamma_0 - \Delta\nu_+)}}{2\gamma_2\zeta}. \qquad (G1)$$

Using the values for ζ, γ_0, γ_1, and γ_2 from this work and the last optical frequency shift measurement $\Delta\nu_+$ from Table II, we find

$$B = 7.000\,076(18) \text{ T}. \qquad (G2)$$

That is, we obtain a measurement of the magnetic field with 2.6 ppm accuracy.

The second method involves measuring the frequency difference $\Delta\nu_+ - \Delta\nu_-$. This method has the advantage that it is not sensitive to the diamagnetic shift and the reference offset, and that it measures about twice the frequency shift compared to first method, i.e., half the relative uncertainty. For these reasons, it is more accurate. The disadvantage is that it requires two probes in the magnetic field and, as such, only works for highly homogeneous fields. The magnetic field is calculated, using Eq. (22), as

$$B = \frac{\Delta\nu_+ - \Delta\nu_-}{2\gamma_1\zeta}. \qquad (G3)$$

Using the values for ζ and γ_1 from this work and the last optical frequency difference measurement $\Delta\nu_+ - \Delta\nu_-$ from Table II, we find

$$B = 7.000\,0727(46) \text{ T}. \qquad (G4)$$

That is, we obtain a measurement of the magnetic field with 0.7 ppm accuracy.

APPENDIX H: EXPERIMENTAL OBSERVATION OF THE LINE SPLITTING

The transition from the Zeeman regime to the hyperfine Paschen-Back regime for $\sigma_\pm$ lines, as shown in Fig. 2, is experimentally verified by recording spectra at different magnetic field strengths from 0 T to 1.5 T in steps of 0.1 T, as shown in Fig. 18. For this process, we have used
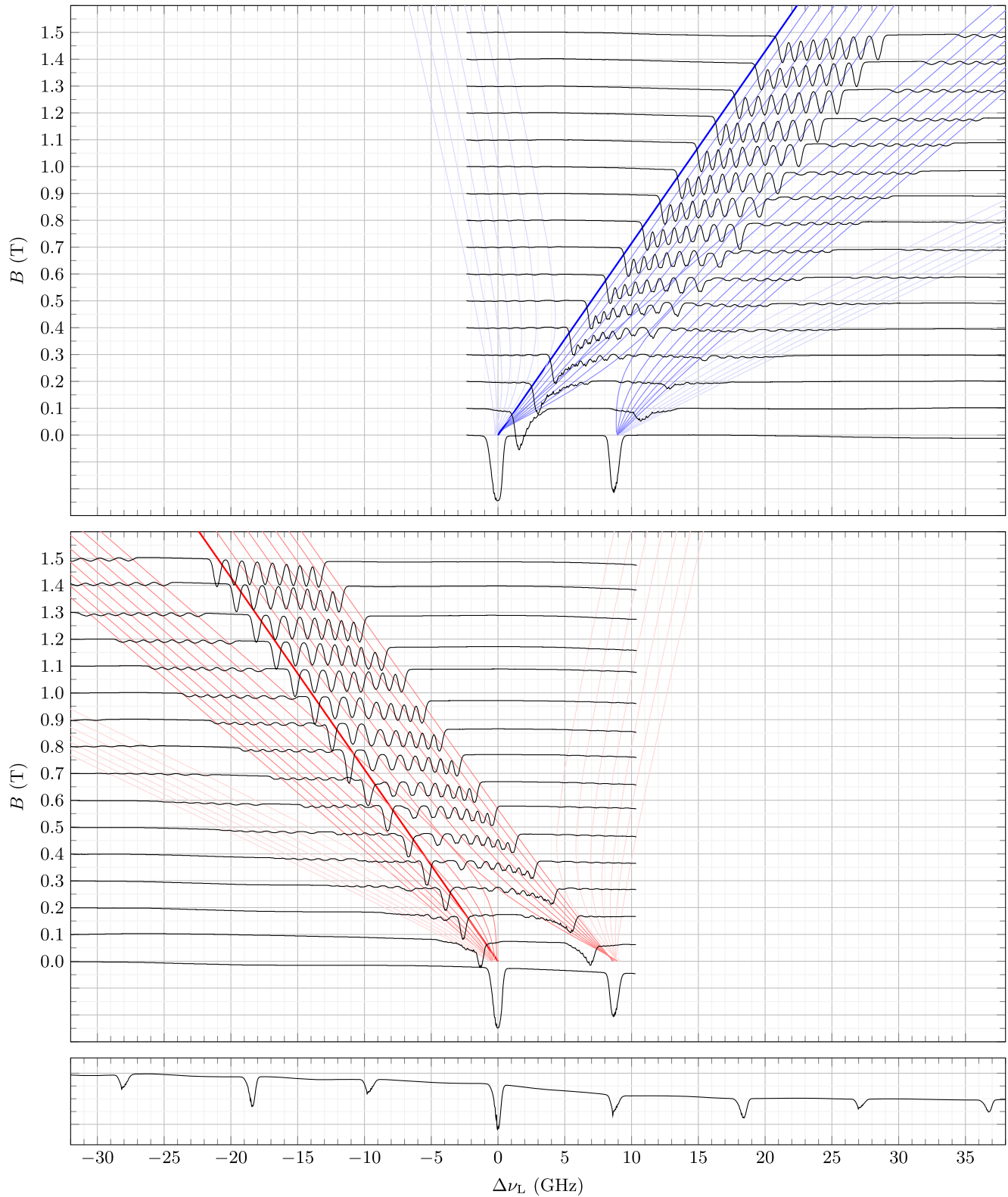
FIG. 18.   Experimental verification of the line splitting using different probe positions outside the 7 T MRI scanner coil. In the upper plot σ_+ polarization is used, and in the middle plot σ_- polarization is used. In the lower plot, the reference probe at 0 T, having sidebands of 18.386 GHz, is used to determine the frequency axis, assuming a linear laser frequency scan $\Delta\nu_L$. The calculated lines are overlaid on top of the spectra. Notice that the axes are flipped, compared to Fig. 2. We see good agreement with the calculated lines.

different probe positions outside the 7 T MRI scanner coil. The magnetic field is 1.5 T near the coil opening and drops to 0.1 T about a meter away from the coil. Notice that the poor field homogeneity eliminates the saturated absorption peaks above 0.6 T.

Each transmission spectrum is displayed in arbitrary units on the *B* axis, according to the magnetic field at which it was obtained. The theoretical lines are overlaid and show good agreement. Notice that the axes are flipped compared to Fig. 2.

The frequency axis is determined with the reference probe at 0 T, with sidebands of 18.386 GHz, using knowledge of the hyperfine structure and assuming a linear frequency scan. The reference spectrum is shown in the bottom of the plot. For these measurements, the EOM shown in Fig. 5 is moved to the beam path going to the reference instead of probes 1–4. Since the laser frequency scan is limited to about 20 GHz, each spectrum is actually two scans stitched together (and the reference spectrum is made from four scans). As the magnetic fields are approximate, and the frequency axis is only approximately linear, these data are primarily meant to verify the pattern of the line splitting.

More rigorous studies at field strengths up to 0.845 T can be found in Refs. [58–60]. These studies also find good agreement between theory and data, and additionally analyze differences and changes in transition strengths. Because of the nonlinear nature of saturated absorption spectroscopy, the absorption depths in Fig. 18 do not accurately represent the relative transition strengths.

---

[1] D. Budker and M. Romalis, *Optical Magnetometry*, Nat. Phys. **3**, 227 (2007).

[2] G. Lembke, S. N. Erné, H. Nowak, B. Menhorn, A. Pasquarelli, and G. Bison, *Optical Multichannel Room Temperature Magnetic Field Imaging System for Clinical Application*, Biomed. Opt. Express **5**, 876 (2014).

[3] R. M. Hill, E. Boto, M. Rea, N. Holmes, J. Leggett, L. A. Coles, M. Papastavrou, S. K. Everton, B. A. E. Hunt, D. Sims *et al.*, *Multi-Channel Whole-Head OPM-MEG: Helmet Design and a Comparison with a Conventional System*, NeuroImage **219**, 116995 (2020).

[4] J. U. Sutter, O. Lewis, C. Robinson, A. McMahon, R. Boyce, R. Bragg, A. Macrae, J. Orton, V. Shah, S. J. Ingleby *et al.*, *Recording the Heart Beat of Cattle Using a Gradiometer System of Optically Pumped Magnetometers*, Comput. Electron. Agric. **177**, 105651 (2020).

[5] M. E. Limes, E. L. Foley, T. W. Kornack, S. Caliga, S. McBride, A. Braun, W. Lee, V. G. Lucivero, and M. V. Romalis, *Portable Magnetometry for Detection of Biomagnetism in Ambient Environments*, Phys. Rev. Appl. **14**, 011002(R) (2020).

[6] S. George, N. Bruyant, J. Béard, S. Scotto, E. Arimondo, R. Battesti, D. Ciampini, and C. Rizzo, *Pulsed High Magnetic Field Measurement with a Rubidium Vapor Sensor*, Rev. Sci. Instrum. **88**, 073102 (2017).

[7] D. Ciampini, R. Battesti, C. Rizzo, and E. Arimondo, *Optical Spectroscopy of a Microsized Rb Vapor Sample in Magnetic Fields up to 58 T*, Phys. Rev. A **96**, 052504 (2017).

[8] J. Keaveney, F. S. Ponciano-Ojeda, S. M. Rieche, M. J. Raine, D. P. Hampshire, and I. G. Hughes, *Quantitative Optical Spectroscopy of* ^{87}Rb *Vapour in the Voigt Geometry in DC Magnetic Fields up to 0.4 T*, J. Phys. B **52**, 055003 (2019).

[9] E. Klinger, H. Azizbekyan, A. Sargsyan, C. Leroy, D. Sarkisyan, and A. Papoyan, *Proof of the Feasibility of a Nanocell-Based Wide-Range Optical Magnetometer*, Appl. Opt. **59**, 2231 (2020).

[10] H. Hori, M. Miki, and M. Date, *Paschen-Back Effect of D-Lines in Sodium Under a High Magnetic Field*, J. Phys. Soc. Jpn. **51**, 1566 (1982).

[11] B. A. Olsen, B. Patton, Y.-Y. Jau, and W. Happer, *Optical Pumping and Spectroscopy of Cs Vapor at High Magnetic Field*, Phys. Rev. A **84**, 063410 (2011).

[12] L. Weller, K. S. Kleinbach, M. A. Zentile, S. Knappe, C. S. Adams, and I. G. Hughes, *Absolute Absorption and Dispersion of a Rubidium Vapour in the Hyperfine Paschen-Back Regime*, J. Phys. B **45**, 215005 (2012).

[13] A. Sargsyan, A. Tonoyan, G. Hakhumyan, C. Leroy, Y. Pashayan-Leroy, and D. Sarkisyan, *Atomic Transitions of Rb,* D_2 *Line in Strong Magnetic Fields: Hyperfine Paschen–Back Regime*, Opt. Commun. **334**, 208 (2015).

[14] A. Sargsyan, E. Klinger, G. Hakhumyan, A. Tonoyan, A. Papoyan, C. Leroy, and D. Sarkisyan, *Decoupling of Hyperfine Structure of Cs* D_1 *Line in Strong Magnetic Field Studied by Selective Reflection from a Nanocell*, J. Opt. Soc. Am. B **34**, 776 (2017).

[15] J. Keaveney, C. S. Adams, and I. G. Hughes, *ElecSus: Extension to Arbitrary Geometry Magneto-Optics*, Comput. Phys. Commun. **224**, 311 (2018).

[16] W. D. Phillips, W. E. Cooke, and D. Kleppner, *Magnetic Moment of the Proton in* H_2O *in Bohr Magnetons*, Metrologia **13**, 179 (1977).

[17] W. B. Garn, R. S. Caird, D. B. Thomson, and C. M. Fowler, *Technique for Measuring Megagauss Magnetic Fields Using Zeeman Effect*, Rev. Sci. Instrum. **37**, 762 (1966).

[18] J. T. Banasek, J. T. Engelbrecht, S. A. Pikuz, T. A. Shelkovenko, and D. A. Hammer, *Measuring 10–20 T Magnetic Fields in Single Wire Explosions Using Zeeman Splitting*, Rev. Sci. Instrum. **87**, 103506 (2016).

[19] J. T. Banasek, J. T. Engelbrecht, S. A. Pikuz, T. A. Shelkovenko, and D. A. Hammer, *Measuring 20–100 T B-Fields Using Zeeman Splitting of Sodium Emission Lines on a 500 kA Pulsed Power Machine*, Rev. Sci. Instrum. **87**, 11D407 (2016).

[20] M. R. Gomez, S. B. Hansen, K. J. Peterson, D. E. Bliss, A. L. Carlson, D. C. Lamppa, D. G. Schroen, and G. A. Rochau, *Magnetic Field Measurements via Visible Spectroscopy on the Z Machine*, Rev. Sci. Instrum. **85**, 11E609 (2014).

[21] J. M. Borrero and K. Ichimoto, *Magnetic Structure of Sunspots*, Living Rev. Solar Phys. **8**, 4 (2011).

[22] J. C. del Toro Iniesta, *On the Discovery of the Zeeman Effect on the Sun and in the Laboratory*, Vistas Astron. **40**, 241 (1996).

[23] R. Battesti, J. Beard, S. Böser, N. Bruyant, D. Budker, S. A. Crooker, E. J. Daw, V. V. Flambaum, T. Inada, I. G. Irastorza *et al.*, *High Magnetic Fields for Fundamental Physics*, Phys. Rep. **765–766,** 1 (2018).

[24] O. Schmidt, K. M. Knaak, R. Wynands, and D. Meschede, *Cesium Saturation Spectroscopy Revisited: How to Reverse Peaks and Observe Narrow Resonances*, Appl. Phys. B **59,** 167 (1994).

[25] E. Arimondo, M. Inguscio, and P. Violino, *Experimental Determinations of the Hyperfine Structure in the Alkali Atoms*, Rev. Mod. Phys. **49,** 31 (1977).

[26] D. Steck, *Cesium D Line Data*, https://steck.us/alkalidata/cesiumnumbers.pdf (2019), retrieved July 27, 2022.

[27] V. Gerginov, A. Derevianko, and C. E. Tanner, *Observation of the Nuclear Magnetic Octupole Moment of ^{133}Cs*, Phys. Rev. Lett. **91,** 072501 (2003).

[28] E. Tiesinga, P. J. Mohr, D. B. Newell, and B. N. Taylor, *CODATA Recommended Values of the Fundamental Physical Constants: 2018*, Rev. Mod. Phys. **93,** 025010 (2021).

[29] E. Arimondo, D. Ciampini, and C. Rizzo, *Chapter One— Spectroscopy of Natural and Artificial Atoms in Magnetic Fields*, Adv. At. Mol. Opt. Phys. **65,** 1 (2016).

[30] H. A. Bethe and E. E. Salpeter, *Quantum Mechanics of One- and Two-Electron Atoms* (Springer-Verlag, Berlin, 1957), pp. 209, 214.

[31] G. K. Woodgate, *Elementary Atomic Structure* (Oxford University Press, New York, 1980), pp. 149–150.

[32] P. van der Straten and H. Metcalf, *Atoms and Molecules Interacting with Light* (Cambridge University Press, Cambridge, England, 2016), pp. 181–182, 213.

[33] R. H. Garstang, *Atoms in High Magnetic Fields (White Dwarfs)*, Rep. Prog. Phys. **40,** 105 (1977).

[34] W. Hüttner, P. Otto, and M. Gamperling, *Second-Order Zeeman Effect in the 5^2S-3^2S and 4^2D-3^2S Two-Photon Transitions of Atomic Sodium*, Phys. Rev. A **54,** 1318 (1996).

[35] P. Otto, M. Gamperling, M. Hofacker, T. Meyer, V. Pagliari, A. Stifter, M. Krauss, and W. Hüttner, *Level Magnetizabilities of the Alkaline Metal Atoms*, Chem. Phys. **282,** 289 (2002).

[36] C.-J. Lorenzen and K. Niemax, *Precise Quantum Defects of nS, nP and nD Levels in Cs I*, Z. Phys. A **315,** 127 (1984).

[37] J. S. Tiedeman and H. G. Robinson, *Determination of $g_J(^1H, 1^2S_{\frac{1}{2}})/g_s(e)$: Test of Mass-Independent Corrections*, Phys. Rev. Lett. **39,** 602 (1977).

[38] J. Abele, M. Baumann, and W. Hartmann, g_J-*Factors and Magnetic HFS Interaction Constants in the $6^2P_{3/2}$- and $8^2P_{3/2}$-States of ^{133}Cs*, Phys. Lett. A **51,** 169 (1975).

[39] G. H. Gossel, V. A. Dzuba, and V. V. Flambaum, *Calculation of Strongly Forbidden M1 Transitions and g-factor Anomalies in Atoms Considered for Parity-Nonconservation Measurements*, Phys. Rev. A **88,** 034501 (2013).

[40] H. Stærkind, *Data Underlying: Precision Measurement of the Excited State Lande g-Factor and Diamagnetic Shift of the Cesium D2 Line*, 10.5281/zenodo.7189170 (2023).

[41] C. Barmet, N. D. Zanche, and K. P. Pruessmann, *Spatio-temporal Magnetic Field Monitoring for MR*, Magn. Reson. Med. **60,** 187 (2008).

[42] S. H. Madkhaly, L. A. Coles, C. Morley, C. D. Colquhoun, T. M. Fromhold, N. Cooper, and L. Hackermüller, *Performance-Optimized Components for Quantum Technologies via Additive Manufacturing*, PRX Quantum **2,** 030326 (2021).

[43] M. C. Wapler, J. Leupold, I. Dragonu, D. von Elverfeld, M. Zaitsev, and U. Wallrabe, *Magnetic Properties of Materials for MR Engineering, Micro-MR and Beyond*, J. Magn. Reson. **242,** 233 (2014).

[44] P. J. Mohr and B. N. Taylor, *CODATA Recommended Values of the Fundamental Physical Constants: 1998*, Rev. Mod. Phys. **72,** 351 (2000).

[45] J. F. Schenck, *The Role of Magnetic Susceptibility in Magnetic Resonance Imaging: MRI Magnetic Compatibility of the First and Second Kinds*, Med. Phys. **23,** 815 (1996).

[46] W. M. Haynes, *CRC Handbook of Chemistry and Physics*, 97th ed. (CRC Press, Boca Raton, 2016), Chap. 4, pp. 124, 126–127.

[47] J. G. Bouwman and C. J. G. Bakker, *Alias Subtraction More Efficient than Conventional Zero-Padding in the Fourier-Based Calculation of the Susceptibility Induced Perturbation of the Magnetic Field in MR*, Magn. Reson. Med. **68,** 621 (2012).

[48] J. G. Bouwman, *Forward Field-Shift Calculation for MRI*, https://www.mathworks.com/matlabcentral/fileexchange/37278-forward-field-shift-calculation-for-mri (2014), retrieved May 30, 2022.

[49] K. M. Koch, X. Papademetris, D. L. Rothman, and R. A. de Graaf, *Rapid Calculations of Susceptibility-Induced Magnetostatic Field Perturbations for in vivo Magnetic Resonance*, Phys. Med. Biol. **51,** 6381 (2006).

[50] R. W. Brown, Y.-C. N. Cheng, E. M. Haacke, M. R. Thompson, and R. Venkatesan, *Magnetic Properties of Tissues*, in *Magnetic Resonance Imaging* (John Wiley & Sons, New York, 2014), Chap. 25, pp. 739–777.

[51] B. W. Petley and R. W. Donaldson, *The Temperature Dependence of the Diamagnetic Shielding Correction for Proton NMR in Water*, Metrologia **20,** 81 (1984).

[52] C. J. Foot, *Atomic Physics* (Oxford University Press, New York, 2012), pp. 98, 142, and 144.

[53] *MATLAB, Curve Fitting Toolbox User's Guide*, https://se.mathworks.com/help/pdf_doc/curvefit/curvefit.pdf (2022), retrieved July 27, 2022.

[54] S. A. Fedorov, G. A. Vishnyakova, E. S. Kalganova, D. D. Sukachev, A. A. Golovizin, D. O. Tregubov, K. Y. Khabarova, A. V. Akimov, N. N. Kolachevsky, and V. N. Sorokin, *Improved Measurement of the Hyperfine Structure of the Laser Cooling Level $4f^{12}(^3H_6)5d_{5/2}6s^2(J = 9/2)$ in $^{169}_{69}$Tm*, Appl. Phys. B **121,** 275 (2015).

[55] G. A. Pitz, C. D. Fox, and G. P. Perram, *Pressure Broadening and Shift of the Cesium D_2 Transition by the Noble Gases and N_2, H_2, HD, D_2, CH_4, C_2H_6, CF_4, and ^{3}He with Comparison to the D_1 Transition*, Phys. Rev. A **82,** 042502 (2010).

[56] L. Young, W. T. Hill, S. J. Sibener, S. D. Price, C. E. Tanner, C. E. Wieman, and S. R. Leone, *Precision Lifetime Measurements of Cs 6p $^2P_{1/2}$ and 6p $^2P_{3/2}$ Levels by Single-Photon Counting*, Phys. Rev. A **50,** 2174 (1994).

[57] R. Grimm and J. Mlynek, *The Effect of Resonant Light Pressure in Saturation Spectroscopy*, Appl. Phys. B **49**, 179 (1989).

[58] A. Sargsyan, A. Tonoyan, G. Hakhumyan, A. Papoyan, E. Mariotti, and D. Sarkisyan, *Giant Modification of Atomic Transition Probabilities Induced by a Magnetic Field: Forbidden Transitions Become Predominant*, Laser Phys. Lett. **11**, 055701 (2014).

[59] A. Sargsyan, B. Glushko, and D. Sarkisyan, *Micron-Thick Spectroscopic Cells for Studying the Paschen–Back Regime on the Hyperfine Structure of Cesium Atoms*, J. Exp. Theor. Phys. **120**, 579 (2015).

[60] A. Sargsyan, A. Amiryan, A. Tonoyan, E. Klinger, and D. Sarkisyan, *Coherent Optical Processes on Cs* D_2 *Line Magnetically Induced Transitions*, Phys. Lett. A **434**, 128043 (2022).